A Synthetic Dynamic PVA Photoresin for Ultrafast Volumetric Bioprinting

Wanwan Qiu[1], Jenny Gehlen[1†], Margherita Bernero[1†], Christian Gehre[1], Gian Nutal Schädli[1], Ralph Müller[1]*, and Xiao-Hua Qin[1]*

† Denotes equal contribution

* Corresponding author. E-mail: qinx@ethz.ch and ram@ethz.ch

[1] Institute for Biomechanics, ETH Zurich, Leopold-Ruzicka-Weg 4, 8093 Zurich, Switzerland

Abstract

Tomographic volumetric bioprinting (VBP) enables fast photofabrication of cell-laden hydrogel constructs in one step, addressing the limitations of conventional layer-by-layer biomanufacturing. However, existing biomaterials that fulfill the physicochemical requirements of VBP are limited to gelatin-based photoresins of high polymer concentrations. These printed matrices are often too dense to support 3D cell growth. Here, we report a dynamic resin based on thiol-ene photo-clickable polyvinyl alcohol (PVA) for ultrafast VBP of 3D tissue models within 7-15 seconds. The incorporation of gelatin as a sacrificial thermo-reversible network allows VBP of perfusable hydrogels with PVA contents as low as 1.5%, providing a stress-relaxing environment for fast cell spreading and 3D growth of embedded human mesenchymal stem cells. Additionally, site-specific immobilization of chemical cues inside a PVA hydrogel is achieved by 4D tomographic photopatterning. Altogether, this study introduces a synthetic biomaterial enabling ultrafast VBP of functional hydrogel constructs with well-defined physicochemical properties and unprecedented efficiency.

Introduction

Recent advances in three-dimensional (3D) bioprinting (*1-4*) have witnessed the fabrication of various 3D tissue models for both fundamental and translational research in regenerative medicine. Conventional 3D bioprinting techniques rely on the extrusion of a shear-thinning bioink through a nozzle wherein high level of shear stress may compromise the integrity of embedded stem cells (*5*). Since 3D objects are built sequentially one layer at a time, the fabrication speed of structurally complex tissues is limited. Up until now, layer-by-layer fabrication of soft hydrogels containing a perfusable tubular structure remains difficult because the substrate materials tend to deform when new layers are added. To address these limitations, volumetric bioprinting (VBP) has recently emerged as an enabling technique that utilizes tomographic back-projections to fabricate centimeter-scale cell-laden 3D hydrogel constructs within tens of seconds (*6-8*). In VBP, a 3D object is created in a single step by irradiating a photocrosslinkable resin from multiple angles (Fig. 1A). The computed light patterns, which are generated by a digital light projector (DLP) modulator, are spatially deposited into a rotating glass vial containing the resin. Accumulation of the 3D light dose induces localized solidification of the resin. Given the rotational motion during VBP, high viscosity of the resins is required to stabilize solidified structures.

Since the first report on VBP in 2019 (*6*), there has been increasing interests in developing new bioresins for VBP (*9-10*). For instance, Bernal et al. (*6*) reported a bioresin of 10% gelatin methacryloyl (GelMA) and 0.037% (1.26 mM) Lithium phenyl-2,4,6-trimethylbenzoylphosphinate (LAP) as photoinitiator. By combining VBP at physical state and subsequent photochemical post-curing, stable cell-laden hydrogel structures were fabricated. Increasing polymer concentration enhances the printability but compromises the ability of printed matrices to support 3D cell growth. Very recently, Gehlen et al. developed a soft bioresin of 5% GelMA and 0.05% LAP (1.7 mM) enabling enhanced *in vitro* osteogenic differentiation of human mesenchymal stem cells (hMSC) than the 10% GelMA control (*10*). Rizzo et al. (*9*) reported a thiol-ene resin based on norbornene-functionalized gelatin (*11-13*) and 4-arm poly(ethylene glycol) thiols. Using this resin, free-form hydrogel constructs containing C2C12 myoblasts were printed with good stability. However, all reported bioresins rely on photocurable gelatin derivatives of high polymer concentrations. The printed matrices predominantly exhibit high mechanical stiffness that limits fast cell spreading and 3D cell growth. Using these proteinaceous hydrogels, it is hard to achieve independent control of matrix factors such as stiffness and adhesiveness when compared to synthetic hydrogels (PEG (*14-18*), polyvinyl alcohol (*19-20*), and polyacrylamide (*21, 22*)), which impedes a mechanistic understanding of cell-matrix interactions in VBP. This limitation motivates us to develop a generalizable strategy to expand the application of synthetic biomaterials for VBP.

Herein, we report an efficient synthetic dynamic photoresin based on norbornene-functionalized polyvinyl alcohol (nPVA) for ultrafast VBP of 3D tissue models. By introducing a complementary network based on sacrificial thermo-reversible gelatin, a series of bioresins with varying nPVA content are formulated. When being cooled down to 4°C, these materials form physically crosslinked gels and thus enable VBP independent of nPVA concentration (Fig. 1B). These bioresins are rapidly photocurable via highly efficient radical-mediated thiol-ene click chemistry (Fig. 1C). This property enables ultrafast fabrication of complex perfusable hydrogel constructs by VBP within 7-15 s at extremely low nPVA content down to 1.5%. Importantly, we discovered that the printed matrices exhibit stress-relaxing behavior, which supports fast cell spreading already 2 h after VBP and the formation of 3D bone cellular networks after 14 days of osteogenic differentiation in a soft matrix with 1.5% nPVA. Finally, we demonstrate fast site-specific immobilization of complex chemical patterns within a hydrogel by 4D tomographic photopatterning within seconds, which is unachievable in conventional photoresins (*6, 23-25*).

Results

Design of a Synthetic Dynamic Photoresin for VBP

A resin for VBP needs to combine high viscosity, cell-compatibility and photocrosslinking efficiency. Therefore, we chose to devise a formulation that contains a photocrosslinkable synthetic network that provides a modular 3D environment to embedded cells, as well as a sacrificial thermo-reversible network which enables printability. A fully synthetic hydrogel precursor, nPVA, was used to form a covalently crosslinked network with the advantages of low cost, ease of synthesis, modularity, and high reactivity for thiol-ene step-growth photopolymerization (*20, 26, 27*). Recently, Ouyang et al. (*28*) reported a universal strategy to mix gelatin with a variety of inks (alginate, PEG acrylates, hyaluronan, GelMA) for extrusion bioprinting. We reason that the incorporation of sacrificial gelatin into a synthetic hydrogel and its subsequent thermal liberation at 37°C will greatly expand the scope of resins suitable for VBP and render the printed environments more permissive for 3D cell growth. To this end, we devised a printing method that relies on three key steps: cooling-induced gelation of the resin, tomographic photocrosslinking in accordance with computer-aided design (CAD) models, and eventually thermal liberation of gelatin at 37°C (Fig. 1B). Off-stoichiometric thiol-norbornene crosslinking between nPVA and PEG di-thiol (thiol:ene = 4:5) was performed so as to retain the excessive amount of norbornene groups for biofunctionalization. A cysteine-containing fibronectin-derived RGD peptide (CGRGDS) was added to promote cell attachment, whereas LAP (*29*) was selected as the photoinitiator due to its

cytocompatibility and high initiation efficiency. Therefore, the printability and physicochemical properties of our resins could be independently controlled (table S1), enabling us to create dynamic hydrogel environments.

Rheological and Physical Properties of PVA Hydrogels

To investigate the effect of gelatin inclusion, we measured the rheological properties of a resin containing 2% nPVA (Mix 3, Table 1) and 5% gelatin in a temperature sweep between 37°C and 4°C. The resin exhibited a complex modulus of ~3 Pa at 37°C and underwent sol-gel transition at ~18°C. The temperature-dependent complex modulus could reach 1000 Pa to form a physical gel (storage modulus G' >> loss modulus G'') when being chilled to 4°C (Fig. 2A), which underlines its suitability for VBP. In contrast, the rheological properties of 2% nPVA resin solution without gelatin showed a complex modulus of only ~1 Pa during the temperature sweep. These results confirm that the inclusion of gelatin indeed enables the printability of nPVA resins in VBP. Next, we devised a multistep rheological test to mimic the volumetric printing process. As shown in Fig. 2B, the resin exhibited a low shear modulus at a temperature above ~25°C (G' < 2 Pa) but underwent a rapid sol-gel transition upon cooling of the testing system to 20°C. The G' increased to about 1000 Pa when the temperature was decreased to 4°C (G'' ~ 10 Pa). At this point, *in situ* UV irradiation was applied to induce the crosslinking via radical-mediated thiol-ene photopolymerization, which initiated a rapid increase in shear moduli (G' > 6000 Pa, G'' ~ 40 Pa). Finally, a temperature ramp was used to liquefy the gelatin component by thermal disassembly of the gelatin network, which was confirmed by a slow decrease in both G' and G'' when heating the stage to 37°C (Fig. 2B, fig. S1).

The physical properties of nPVA hydrogels were systematically investigated in comparison with a reference hydrogel (10% GelMA) in terms of photo-reactivity, compressive moduli, mass swelling ratio and viscoelasticity as a factor of gelatin release. Photo-rheology results (fig. S2) show that the resins are photocrosslinkable in a wide range of nPVA concentrations (1% - 4%). Although 1% nPVA (Mix 1) appeared to be curable, the gels collapsed after 24 h incubation in PBS at 37°C. Nevertheless, the gels from a 1.5% nPVA resin remained stable after incubation. The physical properties of nPVA hydrogels can easily be tuned by adjusting the polymer content from 1.5% to 4% (fig. S2). Both G' and G'' increased with the increase of nPVA concentration (Table 1). By raising the nPVA concentration from 1.5% to 3%, the compressive modulus (E) increased from ~6.7 kPa to 27 kPa, whereas the mass swelling ratio significantly decreased from 50 to 35. Compared to the reference, nPVA hydrogels are significantly softer and show a much higher degree of water-uptake (Fig. 2C, fig. S3A).

To study the impact of gelatin release, we measured the compressive moduli of different nPVA hydrogels either directly after UV curing (Fig. 2C, 0 h) or following incubation at 37°C for 24 h and 7 days, respectively. The compressive moduli of nPVA hydrogels decreased with the increase of incubation time. For instance, the compressive moduli of 1.5% nPVA gels decreased significantly from 6.7 kPa to 2.7 kPa after 7 days incubation at 37°C. It is assumed that the decrease of compressive modulus is caused by the release of gelatin and network swelling. To test the kinetics of gelatin release, we performed a colorimetric assay of nPVA hydrogels containing fluorescein-labeled gelatin as a reporter. After 24 h incubation in PBS at 37°C, approximately 87% and 84% of gelatin were released from the 1.5% (soft) and 3% (stiff) hydrogels, respectively. After 14 days, the percentage increased to 96% and 93%, respectively (fig. S3B). These results confirm that the thermo-reversible gelatin component is indeed sacrificial and releasable.

Next, we investigated if the inclusion of gelatin would have an impact on the viscoelasticity of nPVA hydrogels, and if so, whether the effect would be reversed upon thermal liberation of gelatin. Stress relaxation tests by unconfined compression showed that the incorporation of gelatin confers faster stress relaxation properties immediately after casting. The covalently crosslinked 3% nPVA hydrogels without gelatin were expected to show a mostly elastic behavior and demonstrated a slow stress relaxation time ($t_{0.85}$) of 712.8 ± 188.1 s, whereas the inclusion of gelatin reduced $t_{0.85}$ to 170.4 ± 121.1 s (Fig. 2D). This enhanced viscoelastic behavior was lost after 48 h of incubation at 37°C. The stress relaxation curve of 3% nPVA with gelatin approached the one without gelatin with a significantly increased $t_{0.85}$ of 987.6 ± 293.4 s, while $t_{0.85}$ remained at 709.3 ± 69.0 s for the pure 3% nPVA gels (Fig. 2E-F). This indicates that the gelatin fraction responsible for a temporary increase in stress relaxation properties was cleared from the hydrogels following a 48 h of washing at 37°C. Decreasing the nPVA concentration to 1.5% while keeping the gelatin content constant produced similar initial stress relaxation dynamics and further decreased the initial $t_{0.85}$ to 63.3 ± 15.8 s. Although a decrease in viscoelasticity was observed after 48 h washing and $t_{0.85}$ increased to 104.7 ± 15.2 s, some stress relaxing properties were retained in this composition which could be especially favorable for cell spreading.

Volumetric Printing of Complex Hydrogel Constructs

After testing the physical properties of nPVA hydrogels, we sought to fabricate complex perfusable hydrogel constructs with varying mechanical stiffness. Using a commercial Tomolite printing system, a “Dose Test” was performed to determine the required exposure parameters for printing a resin based on a 2D projection. This function allows measuring the photocrosslinking efficiency of a given resin directly with the light source of the printer to determine the thresholding laser dose.

Below this threshold, the light absorbed by the resin is not sufficient to generate a stable crosslinked network, whereas too high laser doses result in over-exposure (fig. S4). The exposure parameters facilitate screening for the "Optimal Dose" (OD, referring to the light dose [mJ/cm^2] at which the printed structure is most faithful to the designed structure) for VBP. The OD decreased with the increase of nPVA concentration. These results are consistent with the photo-rheology results (fig. S2). Notably, the OD value for a 1.5% nPVA resin is obviously lower than the reference resin (10% GelMA) with the same LAP concentration (Fig. 3D), and a decreased laser dose (~105 mJ/cm^2) is required for crosslinking of a 3% nPVA resin (fig. S4A). The much lower light dose required for nPVA resins represents a remarkable advantage for bioprinting since over-exposure and excessive reactive species may compromise cell viability (*30, 31*).

With this information in mind, we further investigated volumetric printing of complex hydrogel constructs. For potential integration with perfusion bioreactors, a perfusable branch model was printed with a nPVA concentration as low as 1.5% (Fig. 3A) within 14.2 s. By contrast, the reference resin required a longer time (20 s) to print the same model (fig. S4C). The printing time could be further decreased with the increase of nPVA content (Fig. 3E). Furthermore, a complex trabecular bone construct was fabricated within 15.5 s with a polymer concentration of 1.5% nPVA (Fig. 3B, Video S1). It is important to mention that the fabrication of soft hydrogel constructs with low polymer content is important for 3D cell culture since a softer matrix has been shown to be more permissive for 3D cell growth, differentiation, and migration (*32-35*). To characterize the structural fidelity of printed constructs, we employed micro-computed tomography (micro-CT) imaging. Fig. 3C shows 3D renderings of the volumetrically printed constructs with a bifurcation model. The soft and stiff hydrogel constructs had a channel diameter of 1.34 ± 0.18 mm and 1.45 ± 0.02 mm respectively before the bifurcation, which resulted in two smaller channels of 1.02 ± 0.14 mm and 0.94 ± 0.02 mm respectively (fig. S5). These channel diameters are in agreement with the parameters of the 3D stereolithography (.STL) file used for printing. Due to the swelling behavior of printed hydrogel constructs, the width of the printed channels after incubation appears bigger than that of the corresponding CAD model (fig. S5).

Volumetric Bioprinting of Living Hydrogel Constructs

After establishing the printing process parameters, we evaluated the bio-printability of nPVA resins in terms of cell-compatibility. To shed light on how matrix stiffness impacts cell behavior, two groups of bioresins were formulated: 1.5% nPVA and 3% nPVA for the soft and stiff group, respectively. hMSCs as a class of multipotent cells are playing an important role in cell-based tissue engineering (*36*). A live-dead assay showed that hMSC-laden constructs can be fabricated with

high cell viability (~90%) following 2 h, 24 h and 7 days after printing in soft and stiff constructs (Fig. 4A - i, iv, fig. S6). No significant differences were found between different bioresins (Fig. 4B). These results indicate that both the bioresin formulation and printing process were not harmful to the cells.

Actin-nuclei staining results showed that already 2 h after printing the hMSCs rapidly formed protrusions in the soft matrix, while a much lower degree of spreading was observed in the stiff matrix (fig. S7). We reason that the presence of the temporary gelatin network in the matrix and the resulting viscoelasticity (Fig. 2D-F) facilitate fast cell spreading and cell-matrix remodeling. After 1 day of osteogenic differentiation, cells in the soft matrix appeared with a more elongated morphology and even displayed cell-cell contacts, contrary to cells in the stiff matrix (Fig. 4A - ii, v). After 7 days of cultivation, more interconnected cells with long protrusions were observed in the soft matrix, while more single cells with short protrusions were found in the stiff matrix (Fig. 4A - iii,vi, Video S2). Automated dendrite tracking was used to compare the morphological differences of single cells in the soft and stiff matrices. A stellate cell morphology was observed within the soft matrix, whereas cells embedded in the stiff matrix exhibited much shorter protrusions. Over time, cells continued 3D morphogenesis and an interconnected network was observed in the soft matrix after 14 days (Fig. 4D). These results emphasize that matrix mechanics play an important role in regulating cell morphologies after VBP.

Interestingly, the average cell area initially increased between 2 h and 24 h after printing, but then decreased after 7 days (Fig. 4C). This observation implies remarkable morphological changes of bone cells during 3D osteogenic differentiation considering mature bone cells, termed osteocytes, typically have an ellipsoid cell body and long dendrites in native tissues. The transition from an osteoblastic to an early osteocytic phenotype is associated with the reduction of cell area (*37*). Alizarin red staining evidenced mineral deposition within the soft and stiff matrices following 21 days of *in vitro* osteogenic culture (fig. S8A), indicating the progress of matrix mineralization as a hallmark of osteogenic differentiation. No statistical difference between soft and stiff matrices was observed (fig. S8B). Nevertheless, future work to probe the cellular and molecular dynamics in these printed environments is warranted.

Next, we sought to fabricate more complex constructs using the soft bioresin due to its superior permissiveness. As shown in Fig. 5, a perfusable hMSC-laden construct was successfully printed using a branch model within 15 s. Interestingly, cells in the printed branch model could self-organize into irregularly shaped multicellular aggregates and migrate towards the hollow space of the inner channels after printing (fig. S9). Live-cell confocal images revealed that hMSCs formed

smaller aggregates in the smaller channels (C2 and C3) while bigger cell aggregates with round shapes were observed in the larger C1 channel (Fig. 5B-D).

Actin-nuclei staining was used to detail the location and morphology of cell aggregates after 7 days of culture. The cell aggregates aligned with the orientation of the channels. Besides, the spreading of actin-based cell protrusions into all directions from the hMSC aggregates was observed (Fig. 5E-F, fig. S10). No aggregates were found for cells outside the channels (P1) even though they formed local cell-cell contacts (Fig. 5G). We reason that cells surrounding the channels have more access to nutrients, as well as more physical freedom to self-organize into cell aggregates. In addition, these results exemplify that geometrical cues play an important role in generating aligned multicellular systems (*38, 39*). Therefore, our nPVA bioresin in combination with VBP may find future applications in complex tissue engineering.

In biofabrication, 3D construction of hetero-cellular environments will provide the means to better mimic native tissue environments where paracrine signaling is crucial for cell-cell communication and tissue development (*40, 41*). To test if the nPVA bioresins can be used for 3D co-culture applications, we seeded human umbilical vein endothelial cells (HUVECs) into the hollow channels of a 3D printed hMSC-laden construct (printing time = 12 s) to generate a pre-vascularized model. Before co-culture, the hMSC-laden hydrogel construct was osteogenically differentiated for 7 days. After being dispersed in a supportive collagen hydrogel, HUVECs were loaded into the channels, followed by 3D co-culturing for another 3 days (Fig. 5H). Confocal images evidenced the formation of an endothelial layer (Fig. 5I). Taken together, the convergence of nPVA bioresin with ultrafast VBP technique may facilitate future developments of pre-vascularized tissue models.

Volumetric 4D Photopatterning

Finally, we explored if ultrafast tomographic volumetric printing can be utilized to immobilize molecules-of-interest within a preformed hydrogel for potential spatiotemporal control of cell-matrix interactions during 3D culture. We hypothesize that the residual norbornene groups in a nPVA hydrogel formed by an off-stoichiometric crosslinking are accessible for radical-mediated thiol-ene photo-conjugation (*42-45*) by tomographic photopatterning. This patterning process is realized in 3D in three steps as shown in Fig. 6. First, a centimeter-scale hydrogel was generated by tomographic volumetric printing with a 3% nPVA resin (Mix 4). Subsequently, the construct was immersed in a reaction buffer containing thiolated fluorescein (FITC-SH, 0.85 mM) and LAP photoinitiator (1.7 mM). The FITC-SH molecule was immobilized within predetermined 3D regions by performing a second volumetric printing procedure. The printed 3D patterns were

visualized using a fluorescent stereomicroscope after the removal of soluble dye molecules through washing.

A 3D triangular prism was created inside the printed construct through tomographic photopatterning within 15 s. In addition, geometrically complex 3D patterns such as star-shaped cylinder (Fig. 6B) and a free-form helix (Fig. 6C, Video S3) (*46*) were printed within 25 s and 16.3 s, respectively. Of note, a printed cylinder with a line channel could be site-specifically functionalized with the FITC-SH molecule around its channels within 18 s (fig. S11). Given the short patterning time and the cell-friendly light wavelength (405 nm), we reason that the described volumetric 4D photopatterning could open up new possibilities for the fabrication of biomimetic 3D tissue models. Future work can harness this methodology to functionalize distinct parts of the printed matrices to guide cellular behavior and tissue morphogenesis in a spatially and temporally controlled fashion.

Discussion

The ability to rapidly fabricate centimeter-scale tissue and organ mimetics in the laboratory holds the promise to facilitate a variety of basic and translational research in regenerative medicine. VBP has recently emerged as a powerful tool for fast photofabrication of complex cell-laden constructs. However, practical applications of this new technique in functional tissue engineering request advanced biomaterials that fulfill several requirements: high viscosity, low toxicity, high photoreactivity, good printability and the ability to support 3D cell growth and tissue formation after VBP. Existing materials for VBP are predominantly based on gelatin-based photoresins. While gelatin-based resins with high polymer concentration enable high-fidelity VBP, the printed matrices are often remarkably dense and non-permissive to support 3D cell growth. Furthermore, it is hard to separately study the effects of different matrix factors (e.g., stiffness, ligand density) on cell behaviors since gelatin is a denatured protein derived from collagen.

In this study, we developed a synthetic dynamic photoresin based on thiol-ene photo-clickable nPVA for ultrafast VBP within 7-15 seconds to circumvent the limitations of existing materials. The incorporation of a temporary gelatin network enables us to decouple the physicochemical properties of printed matrices from the fabrication process. Using this resin, we successfully fabricated stress-relaxing hydrogel constructs with low polymer concentration that support fast cell spreading and 3D cell growth, osteogenic differentiation of stem cells and matrix mineralization, the formation of aligned multicellular aggregates and co-culture with endothelial cells. This system utilizes highly efficient thiol-norbornene photo-click chemistry to generate tunable hydrogel environments with nPVA concentrations as low as 1.5%. We report, for the first

time, the fast site-specific grafting of chemical cues within preformed hydrogels by tomographic thiol-ene photopatterning. These features are unachievable in conventional gelatin-based resins. In the future, with the recently reported optical-tuning technique to counteract light scattering (*47*), the nPVA resins may even enable high-fidelity VBP of perfusable tissue constructs with higher cell density and maturity when combined with dynamic loading and co-culture strategies. We envisage that the reported synthetic dynamic photoresin may open new applications for fast biomanufacturing of tailored 3D tissue and organ models for regenerative medicine.

Materials and Methods

Synthesis of nPVA

nPVA was synthesized as previously described (*48*).

Volumetric Printing Procedure

Resins were formulated as described in table S1. Briefly, 0.8-1.2 mL of resin was transferred into the printing glass vials (diameter: 10 mm). The vials were chilled at 4°C for 5-10 min to form gels by physical crosslinking of sacrificial gelatin component. Then, printing was carried out on a commercially available Tomolite v1.0 volumetric printer (Readily3D, EPFL Innovation Park, Switzerland) equipped with the latest version of Apparite software (*7*). After printing, the glass vials were warmed to 37°C to remove the unpolymerized resin. Thereafter, the printed object was washed with prewarmed PBS. Printed objects were transferred into a solution containing sodium persulfate (SPS, 5×10^{-3} M) and tris(2,2- bipyridyl) dichlororuthenium(II) hexahydrate (Ru, 0.5×10^{-3} M) for post-curing under a 405 nm LED lamp (Thorlabs, Germany, 10 mW/cm^2) for 5 min. The printed branch constructs were perfused with Alcian blue to facilitate visualization. Constructs were imaged on a Leica M205 FA stereomicroscope coupled with a DFC550 CCD camera for real color imaging.

Micro-computed tomography (micro-CT)

The 3D renderings were obtained with micro-CT scans performed in air with a micro-CT45 device (Scanco Medical, Bassersdorf, Switzerland). Before scanning the water was carefully removed from the channels using tissue papers. The printed constructs were scanned at 45 kVp energy and 177 µA current, using an integration time of 600 ms. The resulting 3D images had a voxel size of 17.2 µm. A Gaussian filter ($\sigma = 1.2$, support 1) was used to reduce noise in the images before converting the grayscale images to binary images using a threshold corresponding to -10 mg hydroxyapatite/cm^3. A negative threshold was needed because the scan was made in air where the minimum value corresponds to ca. -167 mg HA/cm^3. The greatest connected component was

chosen to remove structures not belonging to the printed construct. The low attenuation property of the hydrogel required additional three binary erosion and dilation iterations to smooth the surface. The channel thickness was analyzed by generating a rectangular volume of interest, laying completely within the boundaries of the 3D image, and the distance transformation method (*49*). The image processing was performed using an in-house developed software framework based on Python 3.6.6 (Python Software Foundation) using the SciPy 1.2.0 library and IPL software (V5.42 Scanco Medical). The 3D renderings were generated with ParaView (V5.10.1, Kitware Inc.) and channel widths were evaluated by using ParaView's built-in measurement tools.

Volumetric Bioprinting (VBP) and Cell Culture

The nPVA-gelatin bioresins were prepared as indicated above except the addition of cells and 2 mM CGRGDSP peptide. All components were sterile-filtered (0.2 µm) except the commercially available sterile gelatin (Sigma-Aldrich, cat. no. G2500). Human bone marrow-derived mesenchymal stem cells (hMSC) (pooled donor, Lonza, Switzerland) were harvested at passage 3-4 and resuspended in 0.8 mL of bioresin at a concentration of 5×10^6 cells mL^{-1}. The well-mixed bioresin was transferred into autoclaved glass vials and immediately chilled at 4°C. After printing, the non-crosslinked resin was liquefied at 37°C and the cell-laden hydrogel constructs were retrieved and washed with prewarmed PBS under sterile conditions, followed by cutting the printed constructs into 12 pieces (radius: 3 mm; thickness: 2 mm) for further evaluation. Cell viability was monitored at different time points following cultivation in osteogenic medium composed of Dulbecco's Modified Eagle's Medium (DMEM), 10% fetal bovine serum (FBS), 1% antibiotic-antimycotic solution, ascorbic acid (50 µg/mL), dexamethasone (100 nM) and beta-glycerophosphate (10 mM). Medium was changed every 2 days.

Perfusable Cell-laden Constructs and Co-culture

Perfusable cell-laden constructs were fabricated using the branch CAD model following the standard VBP procedure with a seeding density of 2.5×10^6 hMSCs mL^{-1}. The printed constructs were stained by incubating in Calcein-AM (2 µM) at 37°C and 5% CO_2 for 2 h. Live-cell imaging was performed using a confocal microscope (Leica SP8) after cultivation for 3-4 days.

The hMSC-laden models with hollow channels (diameter = 1 mm) were cultivated in osteogenic medium for 7 days. Constructs were stained in Calcein-AM (2 µM) for 1.5 h at 37°C and 5% CO_2 before seeded with human umbilical vein endothelial cells (HUVECs, pooled donor, Lonza, Switzerland). Endothelial Cell Growth Medium-2 (EGM-2, Lonza, Switzerland) was used as the medium. The harvested HUVECs (passage 3) were labelled with DiD cell labelling solution (Vybrant, Thermo Fisher Scientific), and seeded with a blunt-tip cannula (diameter = 0.8 mm) into

the perfusable channels at a density of 5×10^6 cells mL^{-1} with a supporting collagen type I matrix (Corning, 1 mg/mL). The constructs were cultured in a co-culture medium (1:1 mix of osteogenic medium and EGM-2).

Volumetric 4D Photopatterning

Cylindrical hydrogel constructs were printed using the 3% nPVA resin and washed for 3 days at 37°C. Then the printed cylinders were immersed in a solution containing 0.85 mM FITC-SH and 1.7 mM LAP overnight at 4°C. To improve the stability of thiolated molecules, TCEP (21 mM) and pyrogallol (85 ppm) were added to the working solution. The stained hydrogel constructs were transferred to glass vials to perform volumetric photopatterning by conducting a second printing step, followed by washing in PBS on a shaker for two days to remove non-reacted FITC-SH in the printed constructs. The patterned objects were imaged with a Leica M205 FA stereomicroscope equipped with an X-Cite 200DC lamp with 3 mm light guide and widefield epifluorescence filter sets.

Supplementary Materials

Additional information including the synthesis procedure, hydrogel characterization, photo-rheology measurement, mechanical testing and cellular imaging can be found in the Supplementary Materials document.

References

1. A. C. Daly, M. E. Prendergast, A. J. Hughes, J. A. Burdick, Bioprinting for the Biologist. *Cell* **184**, 18-32 (2021).
2. S. V. Murphy, A. Atala, 3D bioprinting of tissues and organs. *Nat. Biotechnol.* **32**, 773-785 (2014).
3. Y. S. Zhang, G. Haghiashtiani, T. Hübscher, D. J. Kelly, J. M. Lee, M. Lutolf, M. C. McAlpine, W. Y. Yeong, M. Zenobi-Wong, J. Malda, 3D extrusion bioprinting. *Nat. Rev. Methods Primers* **1**, 1-20 (2021).
4. B. Grigoryan, S. J. Paulsen, D. C. Corbett, D. W. Sazer, C. L. Fortin, A. J. Zaita, P. T. Greenfield, N. J. Calafat, J. P. Gounley, A. H. Ta, F. Johansson, A. Randles, J. E. Rosenkrantz, J. D. Louis-Rosenberg, P. A. Galie, K. R. Stevens, J. S. Miller, Multivascular networks and functional intravascular topologies within biocompatible hydrogels. *Science* **364**, 458-464 (2019).
5. A. Blaeser, D. F. Duarte Campos, U. Puster, W. Richtering, M. M. Stevens, H. Fischer, Controlling Shear Stress in 3D Bioprinting is a Key Factor to Balance Printing Resolution and Stem Cell Integrity. *Adv. Healthc. Mater.* **5**, 326-333 (2016).
6. P. N. Bernal, P. Delrot, D. Loterie, Y. Li, J. Malda, C. Moser, R. Levato, Volumetric Bioprinting of Complex Living-Tissue Constructs within Seconds. *Adv. Mater.* **31**, 1904209 (2019).
7. D. Loterie, P. Delrot, C. Moser, High-resolution tomographic volumetric additive manufacturing. *Nat. Commun.* **11**, 852 (2020).

8. B. E. Kelly, I. Bhattacharya, H. Heidari, M. Shusteff, C. M. Spadaccini, H. K. Taylor, Volumetric additive manufacturing via tomographic reconstruction. *Science* **363**, 1075-1079 (2019).
9. R. Rizzo, D. Ruetsche, H. Liu, M. Zenobi-Wong, Optimized Photoclick (Bio)Resins for Fast Volumetric Bioprinting. *Adv. Mater.* **33**, 2102900 (2021).
10. J. Gehlen, W. Qiu, G. N. Schädli, R. Müller, X.-H. Qin, Tomographic volumetric bioprinting of heterocellular bone-like tissues in seconds. *Acta Biomater.* (2022). Doi: 10.1016/j.actbio.2022.06.020.
11. Z. Mũnoz, H. Shih, C. C. Lin, Gelatin hydrogels formed by orthogonal thiol-norbornene photochemistry for cell encapsulation. *Biomater. Sci.* **2**, 1063-1072 (2014).
12. A. Dobos, J. Van Hoorick, W. Steiger, P. Gruber, M. Markovic, O. G. Andriotis, A. Rohatschek, P. Dubruel, P. J. Thurner, S. Van Vlierberghe, S. Baudis, A. Ovsianikov, Thiol-Gelatin-Norbornene Bioink for Laser-Based High-Definition Bioprinting. *Adv. Healthc. Mater.* **9**, 1900752 (2020).
13. B. G. Soliman, G. S. Major, P. Atienza-Roca, C. A. Murphy, A. Longoni, C. R. Alcala-Orozco, J. Rnjak-Kovacina, D. Gawlitta, T. B. F. Woodfield, K. S. Lim, Development and Characterization of Gelatin-Norbornene Bioink to Understand the Interplay between Physical Architecture and Micro-Capillary Formation in Biofabricated Vascularized Constructs. *Adv. Healthc. Mater.* **11**, 2101873 (2022).
14. B. D. Fairbanks, M. P. Schwartz, A. E. Halevi, C. R. Nuttelman, C. N. Bowman, K. S. Anseth, A Versatile Synthetic Extracellular Matrix Mimic via Thiol-Norbornene Photopolymerization. *Adv. Mater.* **21**, 5005-5010 (2009).
15. R. Cruz-Acuña, M. Quirós, A. E. Farkas, P. H. Dedhia, S. Huang, D. Siuda, V. García-Hernández, A. J. Miller, J. R. Spence, A. Nusrat, A. J. García, Synthetic hydrogels for human intestinal organoid generation and colonic wound repair. *Nat. Cell Biol.* **19**, 1326-1335 (2017).
16. D. S. W. Benoit, A. R. Durney, K. S. Anseth, The effect of heparin-functionalized PEG hydrogels on three-dimensional human mesenchymal stem cell osteogenic differentiation. *Biomaterials* **28**, 66-77 (2007).
17. S. Galarza, A. J. Crosby, C. Pak, S. R. Peyton, Control of Astrocyte Quiescence and Activation in a Synthetic Brain Hydrogel. *Adv. Healthc. Mater.* **9**, 1901419 (2020).
18. N. Gjorevski, N. Sachs, A. Manfrin, S. Giger, M. E. Bragina, P. Ordóñez-Morán, H. Clevers, M. P. Lutolf, Designer matrices for intestinal stem cell and organoid culture. *Nature* **539**, 560-564 (2016).
19. R. H. Schmedlen, K. S. Masters, J. L. West, Photocrosslinkable polyvinyl alcohol hydrogels that can be modified with cell adhesion peptides for use in tissue engineering. *Biomaterials* **23**, 4325-4332 (2002).
20. X.-H. Qin, X. Wang, M. Rottmar, B. J. Nelson, K. Maniura-Weber, Near-Infrared Light-Sensitive Polyvinyl Alcohol Hydrogel Photoresist for Spatiotemporal Control of Cell-Instructive 3D Microenvironments. *Adv. Mater.* **30**, 1705564 (2018).
21. J. S. Choi, B. A. C. Harley, The combined influence of substrate elasticity and ligand density on the viability and biophysical properties of hematopoietic stem and progenitor cells. *Biomaterials* **33**, 4460-4468 (2012).
22. B. Trappmann, J. E. Gautrot, J. T. Connelly, D. G. T. Strange, Y. Li, M. L. Oyen, M. A. Cohen Stuart, H. Boehm, B. Li, V. Vogel, J. P. Spatz, F. M. Watt, W. T. S. Huck, Extracellular-matrix tethering regulates stem-cell fate. *Nat. Mater.* **11**, 642-649 (2012).
23. X.-H. Qin, A. Ovsianikov, J. Stampfl, R. Liska, Additive manufacturing of photosensitive hydrogels for tissue engineering applications. *BioNanoMaterials* **15**, 49-70 (2014).

24. T. Gao, G. J. Gillispie, J. S. Copus, A. K. Pr, Y. J. Seol, A. Atala, J. J. Yoo, S. J. Lee, Optimization of gelatin-alginate composite bioink printability using rheological parameters: a systematic approach. *Biofabrication* **10**, 034106 (2018).
25. M. Baumgartner, F. Hartmann, M. Drack, D. Preninger, D. Wirthl, R. Gerstmayr, L. Lehner, G. Mao, R. Pruckner, S. Demchyshyn, L. Reiter, M. Strobel, T. Stockinger, D. Schiller, S. Kimeswenger, F. Greibich, G. Buchberger, E. Bradt, S. Hild, S. Bauer, M. Kaltenbrunner, Resilient yet entirely degradable gelatin-based biogels for soft robots and electronics. *Nat. Mater.* **19**, 1102-1109 (2020).
26. C. E. Hoyle, A. B. Lowe, C. N. Bowman, Thiol-click chemistry: a multifaceted toolbox for small molecule and polymer synthesis. *Chem. Soc. Rev.* **39**, 1355-1387 (2010).
27. B. D. Fairbanks, L. J. Macdougall, S. Mavila, J. Sinha, B. E. Kirkpatrick, K. S. Anseth, C. N. Bowman, Photoclick Chemistry: A Bright Idea. *Chem. Rev.* **121**, 6915-6990 (2021).
28. L. Ouyang, J. P. K. Armstrong, Y. Lin, J. P. Wojciechowski, C. Lee-Reeves, D. Hachim, K. Zhou, J. A. Burdick, M. M. Stevens, Expanding and optimizing 3D bioprinting capabilities using complementary network bioinks. *Sci. Adv.* **6**, eabc5529 (2020).
29. B. D. Fairbanks, M. P. Schwartz, C. N. Bowman, K. S. Anseth, Photoinitiated polymerization of PEG-diacrylate with lithium phenyl-2,4,6-trimethylbenzoylphosphinate: polymerization rate and cytocompatibility. *Biomaterials* **30**, 6702-6707 (2009).
30. S. J. Bryant, C. R. Nuttelman, K. S. Anseth, Cytocompatibility of UV and visible light photoinitiating systems on cultured NIH/3T3 fibroblasts in vitro. *J. Biomater. Sci. Polym. Ed.* **11**, 439-457 (2000).
31. A. Ovsianikov, S. Muhleder, J. Torgersen, Z. Li, X.-H. Qin, S. Van Vlierberghe, P. Dubruel, W. Holnthoner, H. Redl, R. Liska, J. Stampfl, Laser photofabrication of cell-containing hydrogel constructs. *Langmuir* **30**, 3787-3794 (2014).
32. S. J. Bryant, T. T. Chowdhury, D. A. Lee, D. L. Bader, K. S. Anseth, Crosslinking density influences chondrocyte metabolism in dynamically loaded photocrosslinked poly(ethylene glycol) hydrogels. *Ann. Biomed. Eng.* **32**, 407-417 (2004).
33. L. Bian, C. Hou, E. Tous, R. Rai, R. L. Mauck, J. A. Burdick, The influence of hyaluronic acid hydrogel crosslinking density and macromolecular diffusivity on human MSC chondrogenesis and hypertrophy. *Biomaterials* **34**, 413-421 (2013).
34. K. Wolf, M. Te Lindert, M. Krause, S. Alexander, J. Te Riet, A. L. Willis, R. M. Hoffman, C. G. Figdor, S. J. Weiss, P. Friedl, Physical limits of cell migration: control by ECM space and nuclear deformation and tuning by proteolysis and traction force. *J. Cell Biol.* **201**, 1069-1084 (2013).
35. B. Trappmann, B. M. Baker, W. J. Polacheck, C. K. Choi, J. A. Burdick, C. S. Chen, Matrix degradability controls multicellularity of 3D cell migration. *Nat. Commun.* **8**, 371 (2017).
36. X. Xue, Y. Hu, Y. H. Deng, J. C. Su, Recent Advances in Design of Functional Biocompatible Hydrogels for Bone Tissue Engineering. *Adv. Funct. Mater.* **31**, 2009432 (2021).
37. Y. Moharrer, J. D. Boerckel, Tunnels in the rock: Dynamics of osteocyte morphogenesis. *Bone* **153**, 116104 (2021).
38. M. Iannone, M. Ventre, L. Formisano, L. Casalino, E. J. Patriarca, P. A. Netti, Nanoengineered surfaces for focal adhesion guidance trigger mesenchymal stem cell self-organization and tenogenesis. *Nano Lett.* **15**, 1517-1525 (2015).
39. N. Jeger-Madiot, L. Arakelian, N. Setterblad, P. Bruneval, M. Hoyos, J. Larghero, J. L. Aider, Self-organization and culture of Mesenchymal Stem Cell spheroids in acoustic levitation. *Sci. Rep.* **11**, 8355 (2021).
40. G. Rossi, A. Manfrin, M. P. Lutolf, Progress and potential in organoid research. *Nat. Rev. Genet.* **19**, 671-687 (2018).

41. J. A. Brassard, M. Nikolaev, T. Hübscher, M. Hofer, M. P. Lutolf, Recapitulating macro-scale tissue self-organization through organoid bioprinting. *Nat. Mater.* **20**, 22-29 (2021).
42. K. A. Mosiewicz, L. Kolb, A. J. van der Vlies, M. M. Martino, P. S. Lienemann, J. A. Hubbell, M. Ehrbar, M. P. Lutolf, In situ cell manipulation through enzymatic hydrogel photopatterning. *Nat. Mater.* **12**, 1072-1078 (2013).
43. C. K. Arakawa, B. A. Badeau, Y. Zheng, C. A. DeForest, Multicellular Vascularized Engineered Tissues through User-Programmable Biomaterial Photodegradation. *Adv. Mater.* **29**, 1703156 (2017).
44. J. A. Shadish, G. M. Benuska, C. A. DeForest, Bioactive site-specifically modified proteins for 4D patterning of gel biomaterials. *Nat. Mater.* **18**, 1005-1014 (2019).
45. I. Batalov, K. R. Stevens, C. A. DeForest, Photopatterned biomolecule immobilization to guide three-dimensional cell fate in natural protein-based hydrogels. *Proc. Natl. Acad. Sci. U. S. A.* **118**, e2014194118 (2021).
46. X. P. Wang, X.-H. Qin, C. Z. Hu, A. Terzopoulou, X. Z. Chen, T. Y. Huang, K. Maniura-Weber, S. Pané, B. J. Nelson, 3D Printed Enzymatically Biodegradable Soft Helical Microswimmers. *Adv. Funct. Mater.* **28**, 1804107 (2018).
47. P. N. Bernal, M. Bouwmeester, J. Madrid-Wolff, M. Falandt, S. Florczak, N. G. Rodriguez, Y. Li, G. Größbacher, R. A. Samsom, M. van Wolferen, L. J. W. van der Laan, P. Delrot, D. Loterie, J. Malda, C. Moser, B. Spee, R. Levato, Volumetric Bioprinting of Organoids and Optically Tuned Hydrogels to Build Liver-Like Metabolic Biofactories. *Adv. Mater.* **34**, 2110054 (2022).
48. X.-H. Qin, K. Labuda, J. Chen, V. Hruschka, A. Khadem, R. Liska, H. Redl, P. Slezak, Development of Synthetic Platelet-Activating Hydrogel Matrices to Induce Local Hemostasis. *Adv. Funct. Mater.* **25**, 6606-6617 (2015).
49. T. Hildebrand, A. Laib, R. Müller, J. Dequeker, P. Rüegsegger, Direct three-dimensional morphometric analysis of human cancellous bone: microstructural data from spine, femur, iliac crest, and calcaneus. *J. Bone Miner. Res.* **14**, 1167-1174 (1999).
50. D. Loessner, C. Meinert, E. Kaemmerer, L. C. Martine, K. Yue, P. A. Levett, T. J. Klein, F. P. W. Melchels, A. Khademhosseini, D. W. Hutmacher, Functionalization, preparation and use of cell-laden gelatin methacryloyl–based hydrogels as modular tissue culture platforms. *Nat. Protoc.* **11**, 727-746 (2016).

Acknowledgments

The authors would like to thank Drs. Paul Delrot and Damien Loterie (Readily3D) for their generous technical support as well as the staff members of ScopeM at ETH Zurich for their assistance with imaging. Dr. Riccardo Levato (Utrecht University), Dr. Xiaopu Wang and Prof. Bradley Nelson (ETH Zurich) are acknowledged for providing the STL files.

Funding: This project was partially supported by the Swiss National Science Foundation (SNSF) Project funding (No. 188522). X.H. Q. acknowledges the financial support by the SNSF Spark Award (No. 190345). W. Q. gratefully acknowledges financial support from China Scholarship Council (No. 202006790027).

Author contributions:

Conceptualization: X.H.Q.

Methodology: W.Q., X.H.Q., J.G., M.B., G.N.S.

Investigation: W.Q., X.H.Q., J.G., M.B., C.G.

Visualization: W.Q., X.H.Q., G.N.S., M.B.

Supervision: X.H.Q., R.M.

Writing—original draft: W.Q., X.H.Q., M.B.

Writing—review & editing: W.Q., X.H.Q., R.M., M.B., J.G., G.N.S., C.G., G.N.S.

Competing interests: Authors declare that they have no competing interests.

Data and materials availability: All data and materials information are available in the Supplementary Materials.

Figures and Tables

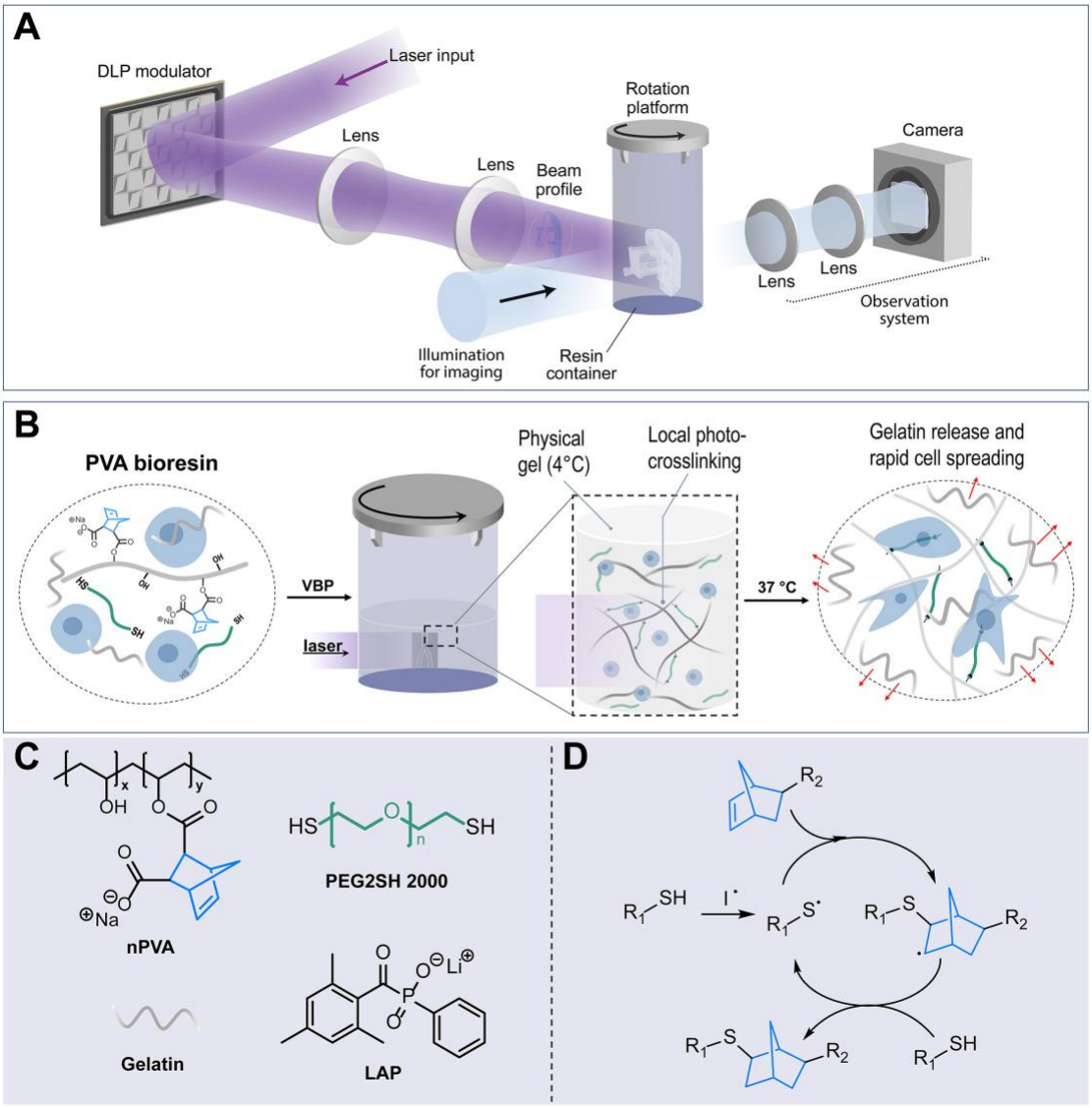

Fig. 1. Design of a synthetic dynamic photo-clickable resin for VBP. (**A**) Schematic of the set-up for VBP. Reproduced under the terms of the CC-BY Creative Commons Attribution 4.0 International license. Copyright 2020, Nature Communications (*7*). (**B**) Illustration of VBP of a PVA bioresin following three steps: cooling-induced solidification of the resin, tomographic photocrosslinking, and thermal liberation of gelatin at 37°C after printing. (**C**) Chemical structures of nPVA, thiolated crosslinker (PEG2SH) and photoinitiator (LAP). (**D**) Mechanism of radical-mediated thiol-norbornene photo-click reaction: the activated initiator generates free radical that abstracts a hydrogen atom from a thiol to give a thiyl radical which propagates across the norbornene C=C bond. The produced norbornane radical abstracts a hydrogen from the thiol group to regenerate a thiyl radical and form a thioether bond.

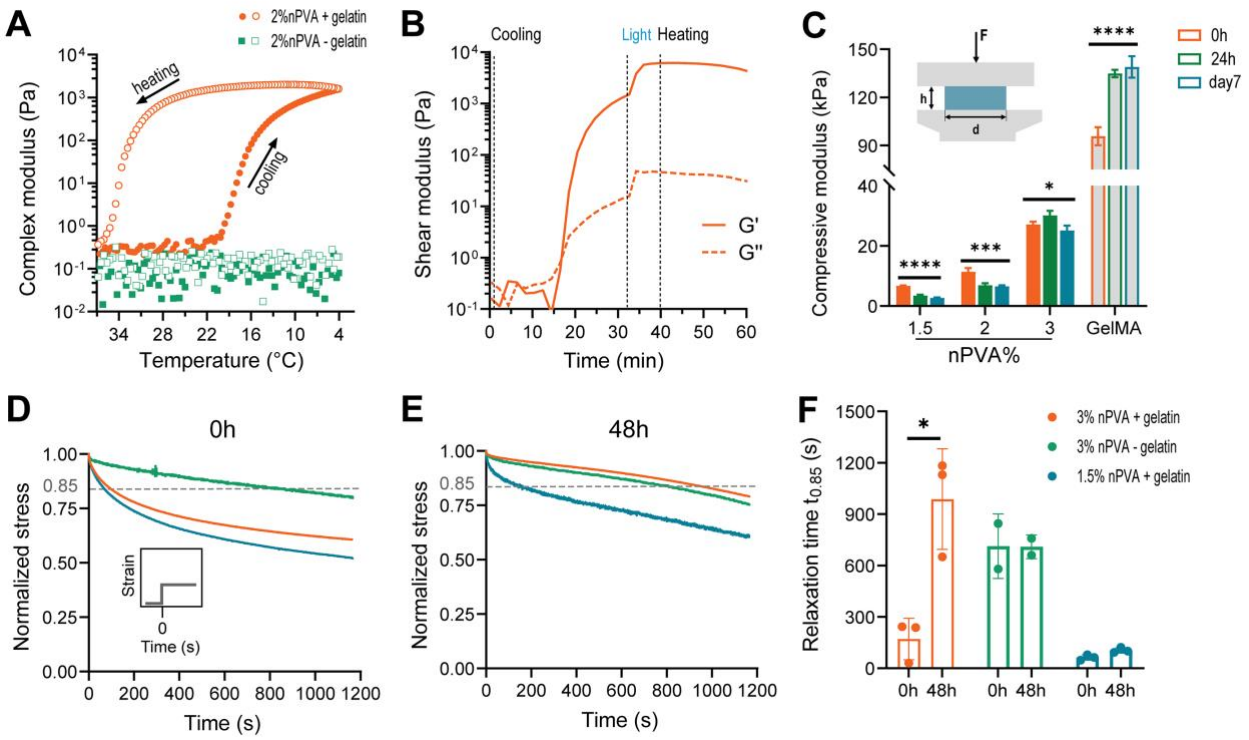

Fig. 2. Rheological and mechanical properties of PVA hydrogels. (**A**) Oscillatory temperature sweep (between 37°C and 4 °C at a rate of 1 °C min^{-1}; closed symbols denote the cooling whereas open ones denote the heating) showing thermo-reversible gelation of a nPVA/gelatin resin, while an undoped 2% nPVA resin exhibits a low viscosity across the range. (**B**) Storage (G') and loss (G'') moduli during a time sweep of a 2% nPVA resin during stages of cooling (from 37°C to 4°C, 1°C min^{-1}), UV light exposure (365 nm, 10 mW/cm^2), and heating back to 37°C. **(C)** The compressive moduli (*E*) of PVA hydrogel disks before (0 day) and following 1 day and 7 days incubation at 37°C. Control: 10% GelMA. Data presented as mean ± standard deviation (SD). *p=0.0136; ***p=0.0009; ****p<0.0001; ns, not significant ($n \geq 3$). (**D-F**) The influence of gelatin on the stress relaxation properties of PVA hydrogels. Means of normalized stress measurements immediately after casting (**D**) and after 48 h of washing (**E**) are shown. The dashed line indicates the cut-off used for quantifying the stress relaxation time $t_{0.85}$. (**F**) Relaxation times $t_{0.85}$ before (0 h) and after washing (48 h). Data presented as mean ± SD. *p<0.05 ($n \geq 2$). The 1.5% nPVA group cannot form a gel without gelatin.

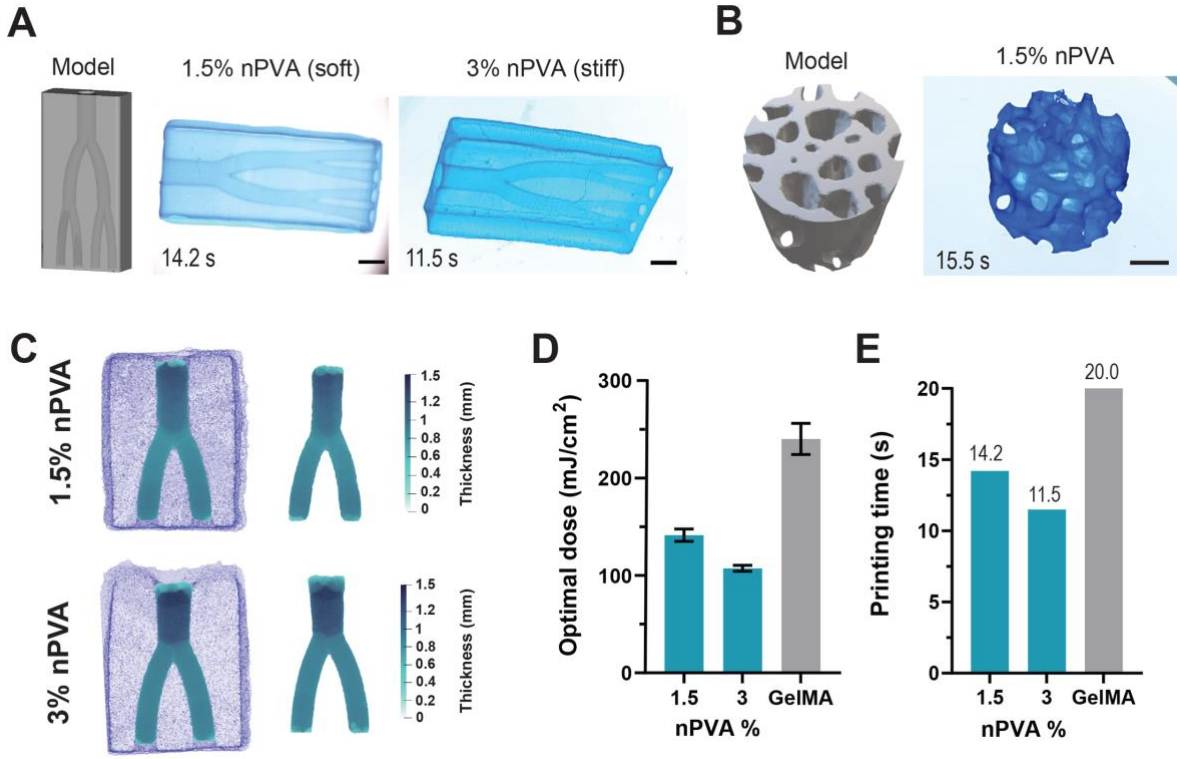

Fig. 3. Volumetric printing of perfusable hydrogel constructs. (**A**) CAD model (left) and stereo-microscopic images (right) of perfusable branch constructs fabricated via volumetric printing using a resin containing 1.5% nPVA and 3% nPVA within 14.2 s and 11.5 s, respectively. LAP concentration was 2 mM. (**B**) CAD model (left) and stereo-microscopic image (right) of a trabecular bone femur construct printed with 1.5% nPVA (printing time = 15.5 s). Scale bars, 2 mm. (**C**) 3D volume reconstruction of printed soft and stiff constructs (left) by micro-CT and quantification of the channel diameters (right). Color coding represents the channel diameter. (**D**) The optimal laser dose of different nPVA resins (reference: 10% GelMA) using the branch CAD model. (**E**) The printing time of different nPVA resins and the reference resin using the branch CAD model.

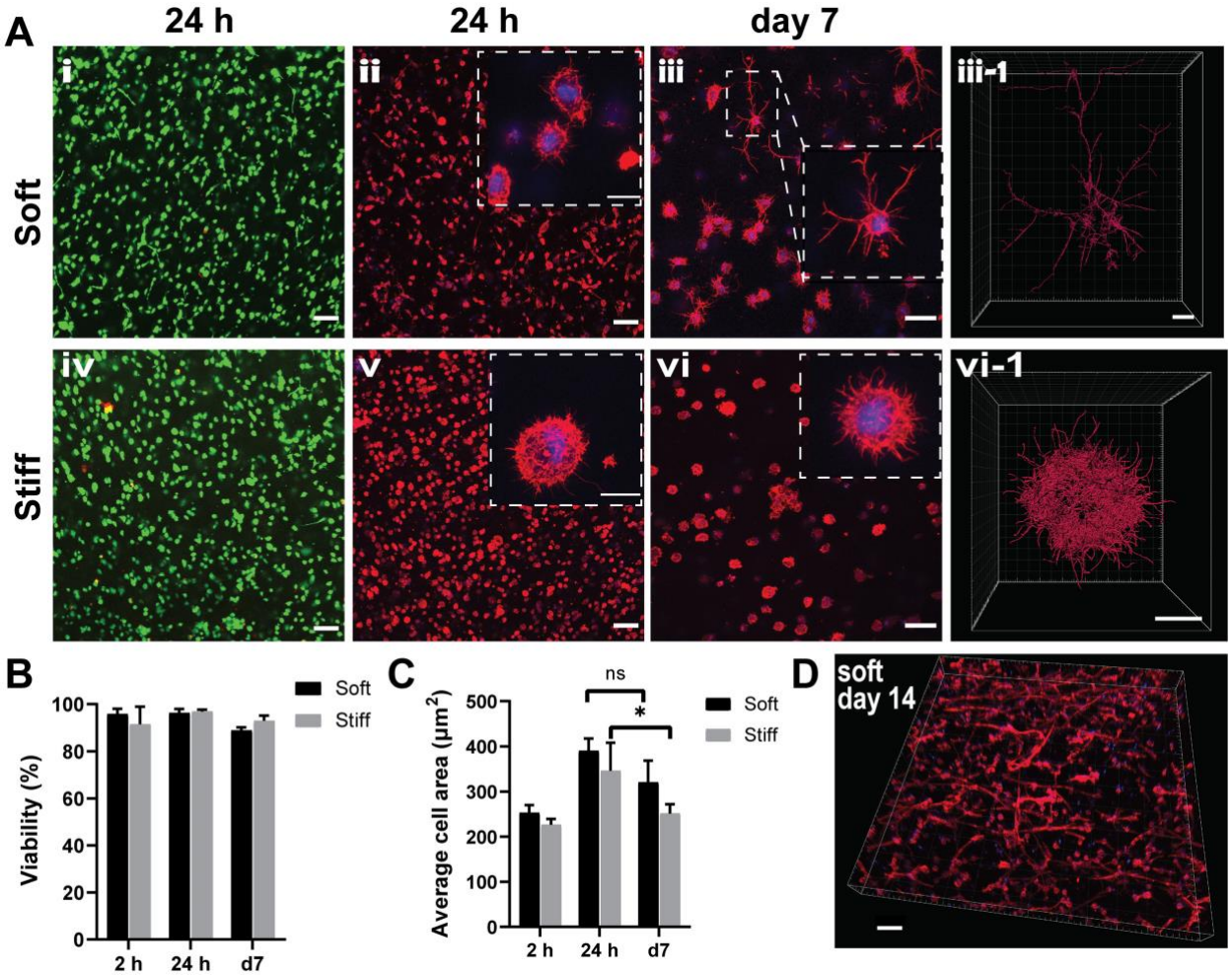

Fig. 4. Cell activity in 3D bioprinted dynamic hydrogel environments of varying stiffness. (**A**) Live(green)/dead(red) stained hMSCs following 24 h after printing. Scale bars, 100 µm (i, iv). Confocal images of actin-nuclei stained hMSCs in soft and stiff gels at 24 h (ii,v) and 7 days (iii, vi) after printing. Scale bars, 100 µm (ii, vi) and 50 µm (iii, vii). Scale bars for all inserts are 20 µm. Visualization of single cells in soft and stiff matrix using automated IMARIS dendrite tracking. Scale bars, 10 µm (iii-1, vi-1). (**B**) Quantification of cell viability of hMSCs at different time points. (**C**) Quantification of average cell area at different time points. *p=0.0268; ns, not significant ($n \geq 3$). (**D**) Confocal image of actin-nuclei stained hMSCs in soft gels following 14 days of osteogenic culture. Scale bar, 100 µm.

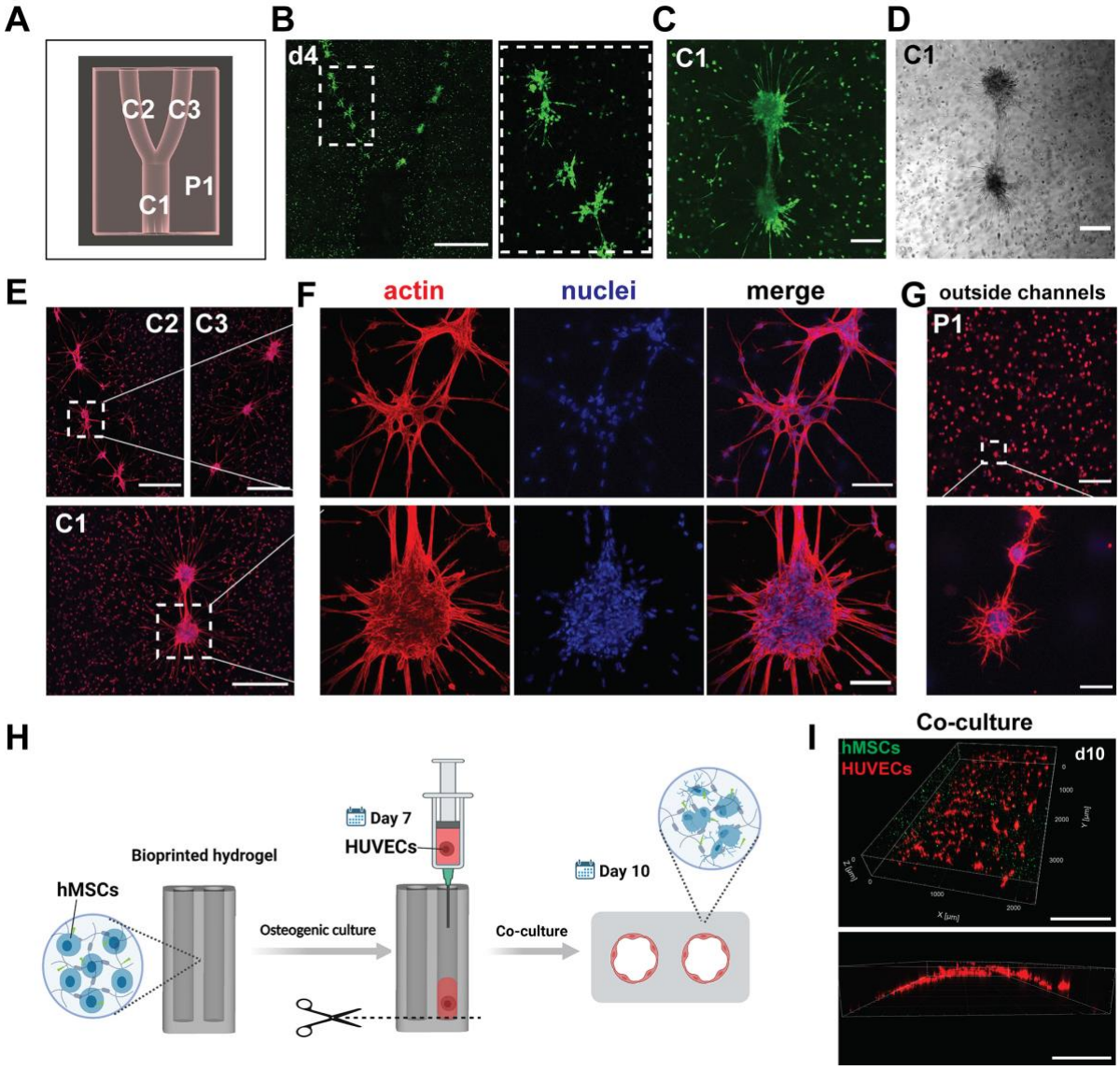

Fig. 5. VBP of perfusable cell-laden constructs. (**A**) The simplified CAD model containing a tubular structure was used for VBP of perfusable constructs. The larger channel C1 splits into the smaller channels C2 and C3, while the surrounding area is referred to P1. (**B**) Confocal images of Calcein AM-stained cells (green) at day 4 in a construct printed from the soft bioresin. Scale bar, 1 mm. (**C-D**) Confocal and bright-field images of Calcein AM-stained cell aggregates adjacent to the big channel (C1) on day 4. Scale bars, 200 µm. (**E**) Confocal images of actin-nuclei stained cell aggregates at positions C2, C3 and C1 on day 7. Scale bars, 500 µm. (**F**) High magnification confocal images of two actin-nuclei stained cell aggregates in the small channels (C2, top) and big channel (C1, bottom). Scale bars, 100 µm. (**G**) Confocal actin-nuclei images of representative cells outside the channels (P1) in the printed construct. Scale bars, 100 µm (top) and 20 µm (bottom). (**H-I**) VBP of a pre-vascularized model. (**H**) Illustration of the experimental steps: Using a custom simplified

CAD model, a hMSC-laden construct is bioprinted and differentiated under osteogenic conditions until day 7. Then, HUVECs in a supporting collagen matrix are injected into the channels. Over time, the collagen hydrogel is remodeled and HUVECs can self-organize into a cell layer in the channels of hMSC-laden constructs after another 3 days. (**I**) Confocal images of hMSCs and HUVECs stained with calcein-AM and DiD, respectively, after co-culture for 3 days. Scale bars, 1 mm.

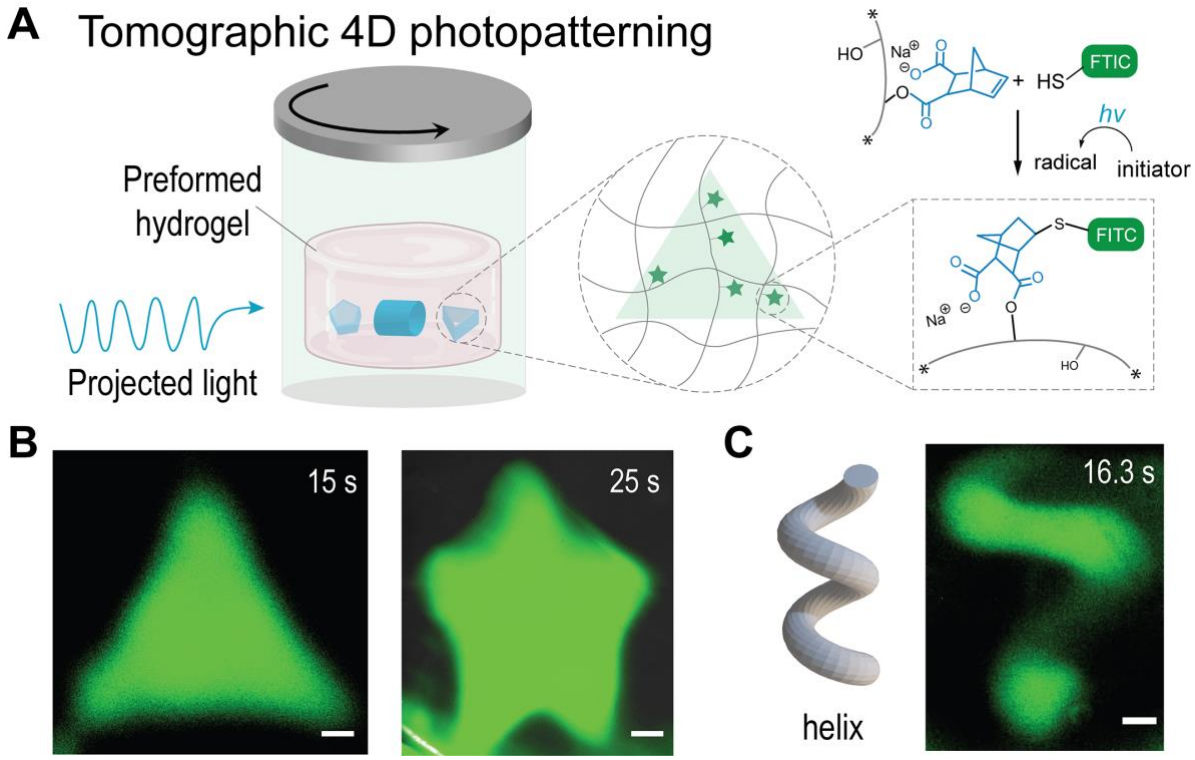

Fig. 6. Volumetric photopatterning of chemical cues in preformed hydrogel constructs within seconds. (**A**) Illustration of volumetric patterning process. (**B**) Top view of fluorescent stereomicroscopy images of a patterned triangular prism and five-star models. (**C**) A complex 3D helix model was patterned within 16.3 s: CAD model (left) and stereomicroscopic image of the patterned construct (right). Scale bars, 500 µm.

Table 1. Physicochemical properties of PVA hydrogels with varying polymer concentration.

Group *	Resin ‡	Storage modulus G' (kPa) §	Loss modulus G'' (Pa) §	Loss factor ($x10^{-3}$) §	Compressive modulus E (kPa) ‖
Mix 1 †	1% nPVA	3.4 ± 0.4	32.0 ± 3.9	9.5 ± 0.3	-
Mix 2	1.5% nPVA	6.6 ± 0.2	56.9 ± 1.4	8.6 ± 0.3	2.7 ± 0.1
Mix 3	2% nPVA	7.5 ± 1.3	56.6 ± 9.4	7.6 ± 0.2	6.6 ± 0.4
Mix 4	3% nPVA	24.0 ± 3.5	131.4 ± 44.4	5.4 ± 1.7	25.1 ± 1.7
Mix 5	10% GelMA	59.7 ± 1.2	954.7 ± 22.9	16.0 ± 0.2	139.0 ± 6.7

*All resins were supplemented with 5% gelatin except Mix 5; † Mix 1 cannot form a stable enough gel; ‡ thiol:ene = 4:5; § Plateau values after *in situ* photocrosslinking for 300 s; ‖ Measured after 7 days incubation in PBS at 37°C.